Printed in the Republic of Korea

ANALYTICAL SCIENCE
& TECHNOLOGY

Vol. 39 No. 1, 22-33, 2026

https://doi.org/10.5806/AST.2026.39.1.22

Alternating laser-ablation data sampling for high-precision laser-induced breakdown spectroscopy analysis: Application to analysis of inorganic mercury dissolved in water

Jangmi Park[1,2], Yonghoon Lee[1,2,3,★], and Sang-Ho Nam[1,★]

[1]Plasma Spectroscopy Analysis Center, Mokpo National University, 1666 Yeongsan-ro, Cheonggye-myeon, Muan-gun, Jeonnam 58554, Republic of Korea

[2]Department of Chemistry, Mokpo National University, 1666 Yeongsan-ro, Cheonggye-myeon, Muan-gun, Jeonnam 58554, Republic of Korea

[3]Department of Energy and Chemical Engineering, Mokpo National University, 1666 Yeongsan-ro, Cheonggye-myeon, Muan-gun, Jeonnam 58554, Republic of Korea

(Received December 8, 2025; Revised December 24, 2025; Accepted December 24, 2025)

Abstract: A high-precision method for quantifying inorganic Hg^{2+} in water was developed by combining strong cation-exchange (SCX) membrane preconcentration with alternating laser-ablation data sampling (ALADS) in laser-induced breakdown spectroscopy (LIBS). Although SCX membranes efficiently captured Hg^{2+}, millimeter scale inhomogeneity of the deposited analyte limited precision when using conventional sampling schemes. ALADS effectively distributed this inhomogeneity across measurement groups, reducing relative standard deviations by almost an order of magnitude. Because the Hg I 253.652 nm resonance line experiences strong self-absorption, the calibration curve exhibited nonlinear saturation behavior. Among three nonlinear models evaluated, the Michaelis–Menten function provided the most accurate and physically meaningful fit. Using ALADS-enhanced precision and the Hg/C intensity ratio, a limit of detection (LOD) of 0.21 mg/kg was achieved—representing a six-fold improvement over analysis without ALADS. Recovery experiments using standard solutions, NIST water CRM, and fortified purified-water samples confirmed the accuracy and matrix tolerance of the approach. While the present configuration provides a practical LOD near 0.2 mg/kg, additional solution-volume preconcentration could extend sensitivity toward the low-ppm or sub-ppm range, enabling applications such as rapid screening of industrial effluents and on-site verification of water-treatment performance.

Key words: laser-induced breakdown spectroscopy (LIBS), inorganic mercury, alternating laser-ablation data sampling (ALADS), solid-phase extraction (SPE), strong cation exchange (SCX) membrane

1. Introduction

Mercury is a unique heavy metal that requires careful analytical attention because its toxicity varies markedly with its chemical forms. Several mercury species pose severe hazards to human health, affecting

---

★ Corresponding author
Phone : +82-(0)61-450-2332, +82-(0)61-450-2333 Fax : +82-(0)61-450-2339, +82-(0)61-450-2339
E-mail : yhlee@mokpo.ac.kr, shnam@mokpo.ac.kr

the central nervous system and kidneys in different ways.[1,2] Elemental mercury vapor (Hg^0) and methylmercury (CH_3Hg^+, MeHg) primarily affect the central nervous system, whereas inorganic mercury species (Hg^+ and Hg^{2+}) tend to accumulate in renal tissues.[3] Because inorganic mercury is more soluble in water and can be transformed into the more toxic MeHg form, its quantification in environmental aqueous matrices remains important for pollution assessment and exposure control. MeHg, the most bioaccumulative mercury species, further underscores the need for reliable mercury monitoring across contaminated aquatic systems.[4]

A wide range of advanced analytical techniques—including inductively coupled plasma–mass spectrometry (ICP-MS),[5] cold vapor atomic absorption spectrometry (CV-AAS),[6] and atomic fluorescence spectrometry (AFS)[7]—provide excellent sensitivity for total mercury determination. However, these techniques inherently lack speciation capability and must be coupled with chromatographic separation, typically high-performance liquid chromatography (HPLC), to distinguish inorganic and organic species.[8,9] Although such hyphenated systems yield exceptional detection limits, they are costly, time-consuming, and require extensive sample preparation, making them unsuitable for rapid screening or on-site measurements.

Solid-phase extraction (SPE) offers a simpler approach for isolating ionic mercury species prior to analysis. Depending on the sorbent chemistry—strong or weak cation exchangers (SCX/WCX) and strong or weak anion exchangers (SAX/WAX)—SPE can selectively retain target species even in complex matrices.[10-12] Importantly, SPE converts dissolved analytes into small solid residues, which are highly compatible with laser-induced breakdown spectroscopy (LIBS). Recent studies have demonstrated that ion-exchange membranes coupled with LIBS can rapidly detect ionic species such as selenium and arsenic.[13,14] LIBS is particularly attractive for this purpose due to its minimal sample preparation without acid digestion, rapid analysis time, and compatibility with solid-phase substrates. In LIBS, a focused nanosecond laser pulse generates a microplasma on the sample surface, and the resulting optical emission contains atomic and ionic lines characteristic of the constituent elements. By dispersing and analyzing these emissions, LIBS enables simultaneous multi-element identification and quantitative determination without complex pretreatment.[15-17]

In this study, we present a simple and rapid method for determining inorganic Hg^{2+} in aqueous samples by integrating an SCX membrane with LIBS. During the membrane-based capture process, however, the retained Hg^{2+} can become distributed non-uniformly across the membrane surface, producing millimeter scale inhomogeneity in the dried solid residues. Such spatial inhomogeneity degrades measurement precision and limits the achievable analytical sensitivity when conventional spot-by-spot sampling is used. To address this issue, we employ an alternating laser-ablation data sampling (ALADS) strategy, which extracts multiple statistically independent measurements from a large set of single-shot spectra by spatially interleaving sampling positions.[18] By averaging spectra collected from distributed locations, ALADS effectively suppresses uncertainty originating from non-uniform analyte deposition. This precision enhancement directly improves detection capability: in our system, the limit of detection (LOD) for inorganic mercury decreased from approximately 2 mg/kg without ALADS to 0.21 mg/kg when ALADS and intensity-ratio calibration were used. In addition to mitigating spatial inhomogeneity, accurate quantification required addressing the strong self-absorption exhibited by the Hg I 253.652 nm resonance line employed as an analyte signal in this study. Because self-absorption induces a pronounced saturation-type nonlinearity in the calibration curve, three nonlinear functions—power-law, exponential saturation, and Michaelis–Menten models—were evaluated. Among them, the Michaelis–Menten model provided the most accurate and physically meaningful description of the calibration behavior, enabling reliable quantification across both low- and high-concentration regimes. Furthermore, the method's robustness was validated through matrix-effect studies, including recovery tests using standard solutions, NIST water CRM spiked with Hg^{2+}, and fortified tap water samples, which collectively demonstrated accurate quantification and negligible matrix interference. Collectively, the integration of SCX-based preconcentration, ALADS-enhanced precision, and nonlinear calibration modeling establishes a practical and species-selective analytical pathway for rapid monitoring of inorganic mercury in contaminated or process-related aqueous samples.

2. Experimental

2.1. Sample preparation

All aqueous solutions were prepared using ultrapure water (18.2 MΩ·cm), produced by a PURELAB plus purification system (PURELAB CLASSIC UV MK2, ELGA, USA). A 1000 mg/kg Hg^{2+} stock solution was prepared from mercury(II) chloride (≥99.5 %, Sigma-Aldrich) and stored at 4 °C. Reagents used for conditioning of the ion-exchange membrane included acetone (≥99.9 %, HPLC grade), methanol (≥99.9 %, HPLC grade), and nitric acid (70 %, ACS reagent grade; all from Sigma-Aldrich). The developed method was further evaluated using NIST SRM 1643f (Trace Elements in Water), to which Hg^{2+} was spiked since the certified material does not contain inorganic mercury. A SCX membrane (Empore™ SPE Disk, 47 mm diameter, 3M Corp., USA), composed of a benzene-sulfonic-acid-functionalized polymer, was used to selectively capture inorganic Hg^{2+} from solution. Prior to use, the membrane was conditioned following the manufacturer's recommended procedure. Briefly, the membrane was fixed on a stainless-steel support screen placed within a Büchner funnel connected to a hand-operated vacuum pump. The membrane was first rinsed with 10 mL acetone at a flow rate of 2 mL/min and fully dried. It was then treated with 10 mL methanol (2 mL/min), followed by 10 mL ultrapure water. Subsequently, 10 mL of 6.3 M HNO$_3$ was passed through the membrane, and finally the membrane was rinsed with 20 mL of ultrapure water, completing the conditioning procedure. *Fig.* 1(a) shows a schematic of the process capturing Hg^{2+} dissolved in standard or sample solutions for LIBS analysis. For sample loading, 10 mL of Hg^{2+} standard solution was passed through the conditioned membrane at a flow rate of 2 mL/min under gentle vacuum. After filtration, the membrane was removed from the holder and dried in an oven at 40 °C for 24 h to ensure dehydration of the captured residue. The dried membranes were analyzed by inductivelycoupled plasma atomic emission spectroscopy (ICP-AES) to ensure the Hg^{2+} capturing efficiency of the SCX membranes.

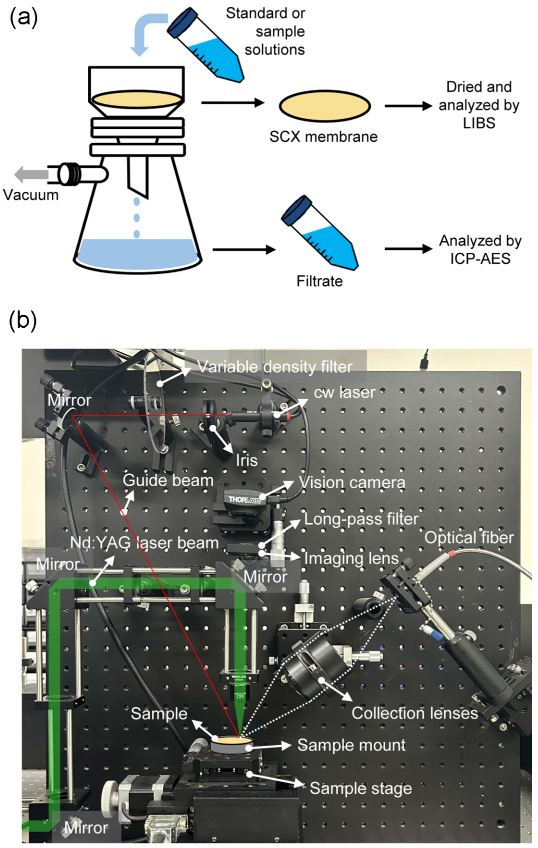

Fig. 1. (a) Sample preparation process and (b) photograph of the laboratory-assembled LIBS setup.

2.2. LIBS analysis

LIBS was employed to analyze the dried SCX membranes containing adsorbed Hg^{2+} ions. A laboratory-assembled LIBS system consisting of a Q-switched Nd:YAG laser (532 nm, <5 ns pulse width, maximum 450 mJ/pulse, Brilliant b, Quantel), a Czerny–Turner spectrometer (DM-500i, Dongwoo Optron), and an intensified CCD (ICCD) detector (1024 × 512 pixels, iStar, Andor Technology) was used. *Fig*. 1(b) shows a photograph of the optical setup. The second-harmonic laser beam was focused onto the membrane surface through an objective lens (5× magnification, 35 mm working distance). For quantitative analysis, a pulse energy of 5 mJ was used for all measurements. Because LIBS precision is strongly affected by fluctuations in plasma temperature arising from variations in the laser energy density at the sample surface, maintaining a constant sample surface height (SSH) during analysis is essential.[19,20] To monitor SSH in real time, a continuous-wave diode laser (635 nm; PL202, Thorlabs) was directed obliquely onto the membrane surface. The beam spot on the membrane surface was imaged through a long-pass edge filter (cut-off: 633 nm, LP02-633RE-25, Semrock) using the objective and relay lenses onto a CMOS vision camera (1.6 megapixels, CS165CU/M, Thorlabs). Any deviation in SSH caused a horizontal displacement of the diode-laser spot in the camera image. Initially, the optimal lens-to-sample distance was determined by maximizing plasma brightness. Thereafter, the diode-laser spot position was continuously monitored throughout the measurements, and the *z*-position of the sample stage was manually corrected whenever a drift was detected, ensuring stable focusing conditions and improved measurement precision. Plasma emission produced by the laser ablation was collected using two plano-convex lenses (2-inch diameter, 7 cm focal length) and delivered to the spectrometer via an optical fiber. The spectrometer, equipped with a 1200 grooves/mm grating blazed at 500 nm and a 10 μm entrance slit, provided a spectral bandwidth of 40 nm and a resolution of 0.045 nm at 435.8 nm.[21] The ICCD gate delay and gate width were set to 0.2 μs and 10 μs, respectively, to optimize signal-to-background ratios. The laser repetition rate was 10 Hz. A total of 1681 single-shot LIBS spectra were collected for each membrane sample. Consecutive laser shots were spaced 1 mm apart, and the sample stage was translated at 5 mm/s to maintain uniform crater spacing and minimize surface damage accumulation. These acquisition parameters ensured consistent ablation conditions across the scanned membrane surface.

2.3. ICP-AES analysis

ICP-AES was used to determine the concentration of inorganic Hg^{2+} remaining in the filtrate after the standard and sample solutions were passed through the conditioned SCX membrane. This measurement was performed to verify whether the SCX membrane quantitatively adsorbed all Hg^{2+} ions present in the original solutions. This verification step was essential for validating the membrane-based separation process prior to LIBS analysis. The filtrate solutions were analyzed using an ICP-AES instrument (SPECTRO Flame Modula, Green, Germany). The plasma was sustained with an RF power of 1400 W, while argon was supplied as the plasma gas at a coolant flow of 15.0 L/min, an auxiliary flow of 1.0 L/min, and a nebulizer flow of 1.0 L/min. A cross-flow nebulizer was used to aerosolize the filtrate solutions before introduction into the plasma. The emission intensity of mercury was monitored at 184.9 nm, which was used as the analytical wavelength for quantifying Hg^{2+} concentration in the filtrate. Calibration standards were prepared from the same Hg^{2+} stock solution used for LIBS sample preparation, and all filtrate measurements were conducted under identical conditions to maintain analytical consistency. For all Hg^{2+} concentrations examined—5, 10, 50, 100, and 200 mg/kg—the filtrate solutions obtained after passing the standards through the SCX membrane were analyzed using the same ICP-AES procedure described above. In every case, the Hg signal in the filtrate was below the detection limit of the ICP-AES instrument (~120 μg/kg), indicating that no discernible amount of Hg^{2+} remained in solution after membrane treatment. This confirms that the SCX membrane quantitatively captured the Hg^{2+} ions from all standard solutions under the conditions used in this study.

3. Results and Discussion

3.1. LIBS spectra and assignments

Fig. 2 presents the LIBS spectra of the SCX membranes loaded with Hg^{2+} solutions of 200, 100, 50, 10, and 5 mg/kg, together with a blank membrane, recorded over the wavelength region of 246.0–255.2 nm.

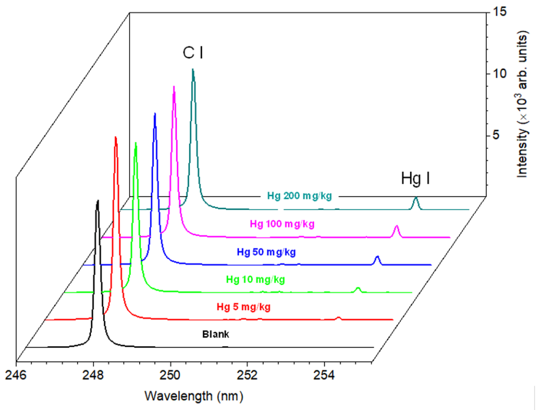

Fig. 2. LIBS spectra of SCX membranes loaded with inorganic Hg^{2+} (5–200 mg/kg) and a blank membrane, showing the Hg I 253.652 nm and C I 247.856 nm emission lines.

Two emission features are clearly observed in this region and were assigned, using the NIST Atomic Spectra Database, to the C I line at 247.856 nm and the Hg I line at 253.652 nm; their spectroscopic parameters are summarized in *Table* 1.[22] The C I emission originates from the benzene-sulfonic-acid-functionalized polymer backbone of the SCX membrane, whose carbon content remains unchanged during the cation-exchange process because only the sulfonic-acid H^+ ions are replaced by Hg^{2+}. Consequently, the C I peak intensity is expected to remain nearly constant regardless of the Hg^{2+} concentration in the sample solution, which is experimentally supported by the low relative standard deviation (RSD) of 9.8 % observed among all membranes including the blank. In contrast, the Hg I 253.652 nm emission increases systematically with increasing Hg^{2+} concentration, while no discernible Hg I emission is observed in the blank membrane, confirming the suitability of this line for quantitative mercury determination. Because of the concentration-independent behavior of the C I emission, the intensity of the Hg I line was normalized to that of the C I line ($I_{\mathrm{Hg\ I}}/I_{\mathrm{C\ I}}$) to improve analytical reliability and compensate for variations arising from pulse-to-pulse fluctuations or minor differences in ablation yield across membrane surfaces. This normalization approach enhanced the consistency of the Hg response and provided a more robust basis for constructing the calibration curves described in the subsequent section.

3.2. Spatial inhomogeneity and limitation of normalization

Fig. 3 displays spatial maps of the Hg I emission intensity ($I_{\mathrm{Hg\ I}}$) for the SCX membranes loaded with Hg^{2+} from standard solutions of 200, 100, 50, 10, and 5 mg/kg (a–e), and the corresponding maps of the normalized intensity ratio ($I_{\mathrm{Hg\ I}}/I_{\mathrm{C\ I}}$) (f–j). For the upper-row panels (a–e), a common intensity scale is shown beside *Fig.* 3(e), whereas a separate common scale for the ratio maps (f–j) is provided next to *Fig.* 3(j). The Hg I intensity maps (a–e) reveal that the captured Hg^{2+} is not uniformly distributed across the membrane surface. In addition to the evident millimeter scale variations across each membrane, the left-upper region consistently exhibits slightly higher emission intensities. This localized enhancement is attributed not to differences in Hg loading but rather to a subtle tilt of the sample stage. Even a small degree of inclination can induce a slight variation in the lens-to-sample distance, positioning the left-upper region closer to the focal point of the laser and thus generating plasmas with marginally higher temperatures and emission intensities. The lower-row maps (f–j) were constructed by normalizing the Hg I intensity to the C I 247.856 nm emission, which

Table 1. Spectroscopic parameters of the C I and Hg I emission lines used in this study. λ is the transition wavelength; A_{ki} is the Einstein spontaneous emission coefficient for the transition from the upper level k to the lower level i; E_{i} and E_{k} denote the lower- and upper-level energy values, respectively; and g_{i} and g_{k} represent the corresponding statistical weights of the lower and upper states.

Species	λ (nm)	A_{ki} ($\times 10^7$ s^{-1})	E_{i} (cm^{-1})	E_{k} (cm^{-1})	g_{i}	g_{k}
C I	247.856	2.8	21648.03	61981.83	1	3
Hg I	253.652	0.840	0.00	39412.24	1	3

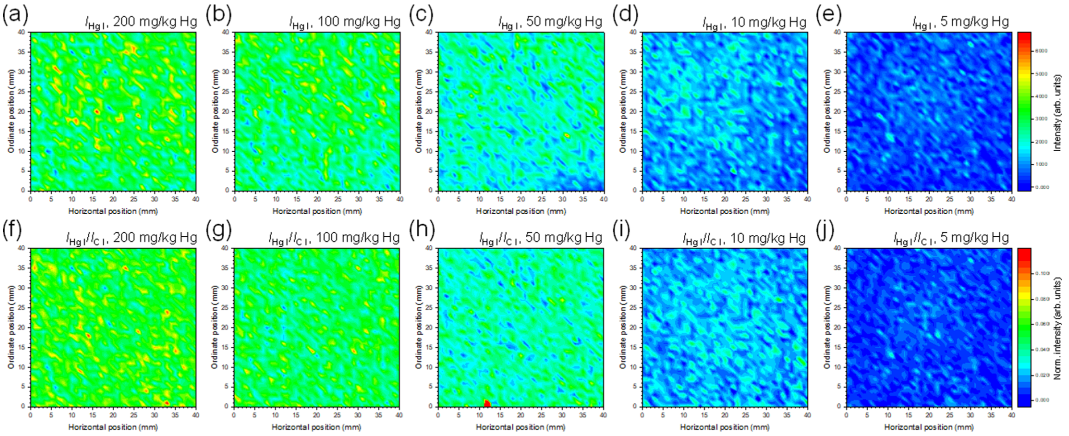

Fig. 3. Spatial maps of (a–e) $I_{\mathrm{Hg\,I}}$ and (f–j) $I_{\mathrm{Hg\,I}}/I_{\mathrm{C\,I}}$ for SCX membranes loaded with Hg^{2+} at 5–200 mg/kg.

originates from the benzene-sulfonic-acid-functionalized polymer matrix of the SCX membrane. Because the carbon content of the membrane remains constant regardless of Hg^{2+} concentration, the C I line provides an effective reference for correcting fluctuations caused by plasma temperature variations or changes in ablation efficiency. Consistent with this expectation, the left-upper intensity enhancement observed in *Figs*. 3(a)–3(e) becomes noticeably reduced in the normalized maps, supporting the interpretation that this feature arises from optical-geometric effects rather than from localized variations in Hg loading.

However, despite this partial correction, the millimeter scale spatial inhomogeneity remains clearly visible in the normalized maps. This persistence indicates that normalization cannot compensate for the inherent irregularities created during the membrane-based capture and drying processes. To quantitatively assess these spatial variations, the RSD values of the 1681 point-wise measurements were calculated for each membrane sample. For membranes loaded with 200, 100, 50, 10, and 5 mg/kg Hg^{2+}, the RSDs of the raw Hg I intensities were 29.6%, 30.2%, 35.8%, 48.0%, and 75.4%, respectively. When normalized to the C I line, the corresponding RSD values were 24.7%, 26.7%, 40.9%, 43.2%, and 75.6%. Although normalization slightly reduced RSD at higher Hg loadings—consistent with its role in correcting plasma-related fluctuations—the overall magnitude of the RSDs remains high, confirming that normalization does not mitigate the dominant contribution from millimeter scale sample inhomogeneity. These results demonstrate that C I normalization effectively compensates for laser-focusing-related temperature variations but does not correct the intrinsic spatial distributional irregularities of Hg across the membrane. Consequently, normalization alone cannot achieve the precision required for high-quality quantitative LIBS analysis. To overcome this limitation, the following section introduces the ALADS method, which we previously developed to suppress sampling-inhomogeneity effects[18] and which proves highly effective in reducing variance and improving analytical precision for Hg determination in SCX membranes.

3.3. ALADS strategy and its precision-enhancing effect

As demonstrated in Section 3.2, the SCX membranes exhibit spatial variations in Hg distribution on the order of a few millimeters, and this millimeter–scale inhomogeneity strongly limits the precision obtainable from conventional single-shot LIBS measurements. Although normalization to the C I line partially compensates for plasma-related fluctuations, it does not correct this intrinsic spatial irregularity. To overcome this limitation, we adopted the ALADS data sampling scheme, previously introduced to suppress sample-inhomogeneity effects in LIBS analysis of edible salts.[18] As mentioned above, each SCX membrane in the present work was measured at 1681 equally spaced grid positions (41 × 41 array) with a fixed inter-spot spacing of 1 mm. The single-shot spectra acquired at these positions were labeled sequentially from 1 to 1681. Because the data points are uniformly distributed across the membrane surface, an alternating grouping of the single-shot spectra to form three measurements (e.g., $k = 1, 4, 7, \ldots, 1681$; $k = 2, 5, 8, \ldots, 1679$; and $k = 3, 6, 9, \ldots, 1680$, with k as the index of each laser-ablation sampling point) ensures that each group samples the entire membrane area in an evenly distributed manner. Consequently, each group experiences nearly the same millimeter scale inhomogeneity, and the averaged spectrum of each group constitutes an independent measurement that is statistically equivalent in terms of analyte distribution. The number of groups plays a crucial role. Although at least three groups are required to obtain statistically meaningful precision estimates, increasing the number of groups beyond three becomes counterproductive. As the number of groups increases, the distance between data points assigned to different groups grows larger, preventing each group from sampling the millimeter scale inhomogeneity in an equivalent manner. Consequently, the averaged spectra of different groups begin to reflect different portions of the spatial variability, leading to increased variance among the measurements. To minimize this effect, the number of groups must be kept as small as possible—three in this study—so that the data points distributed across different groups remain closely spaced and the a-few-millimeter inhomogeneity of the membrane surface is equally represented in all groups. Therefore, dividing the 1681 data points into three alternating groups represents the optimal balance, loading the sample inhomogeneity almost equally to each data group while satisfying the requirement for multiple measurements.

To clearly demonstrate the benefit of ALADS, the results obtained using this method were compared with those produced by a sequential data sampling (SDS) scheme. In SDS, the 1681 single-shot spectra were divided into three consecutive groups (k = 1–560, 561–1120, and 1121–1681). Although the mean intensities obtained from SDS and ALADS are identical—because both methods use all data points—the precision differs markedly. In SDS, each group corresponds to a spatially contiguous region of the membrane, and thus the three SDS groups experience different degrees of mm-scale inhomogeneity, yielding noticeably different averaged intensities and substantially larger standard deviations. In contrast, ALADS distributes this spatial inhomogeneity uniformly across the three groups, leading to nearly identical averaged intensities and drastically reduced variance. The improvement is quantitatively illustrated in *Fig.* 4, which compares the RSDs from SDS and ALADS based on three measurements each. Normalization of the Hg I intensity to the C I line provides a modest reduction in RSD, indicating that C I referencing compensates for plasma-related fluctuations to some extent. However, the dominant improvement in precision results from the ALADS scheme. For example, for the membrane loaded with Hg^{2+} from the 5 mg/kg solution, the SDS-based RSD of the Hg I intensity is approximately 10 %, whereas ALADS reduces this value to ~1.5 %, representing more than a six-fold enhancement in precision. Similar improvements are ommbserved for 10, 50, 100, and 200 mg/kg samples, where ALADS consistently yields the smallest RSD values for both the absolute intensity

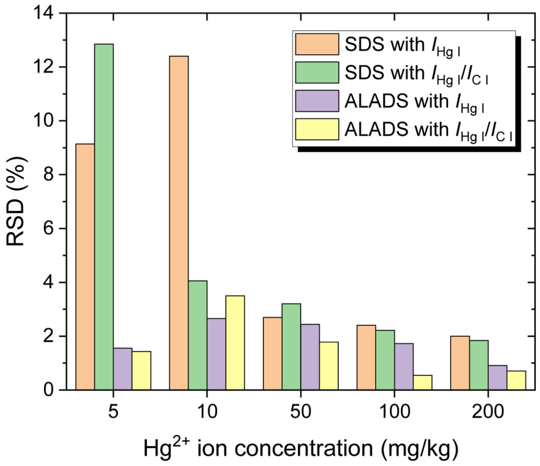

Fig. 4. RSDs of $I_{Hg\ I}$ and $I_{Hg\ I}/I_{C\ I}$ from three measurements obtained by SDS and ALADS schemes.

($I_{\mathrm{Hg\,I}}$) and the intensity ratio ($I_{\mathrm{Hg\,I}}/I_{\mathrm{C\,I}}$). These results clearly show that C I normalization alone cannot correct for spatial inhomogeneity, whereas ALADS directly suppresses the contribution of millimeter scale analyte nonuniformity to the measurement variance. By averaging the spectra within each alternating group, three independent measurements were obtained for every SCX membrane, each reflecting essentially the same spatial heterogeneity. As a result, the variance among the measurements is dramatically reduced compared with that obtained from raw single-shot data, simple normalization, or sequential data grouping. This ALADS-based grouping effectively eliminates the influence of sample inhomogeneity on the measurement variance and provides the foundation for the high precision achieved in the subsequent quantitative calibration.

3.4. Calibration modeling and impact of self-absorption

Fig. 5 presents the calibration curves constructed using the average of the three measurements obtained from either SDS or ALADS sampling. Because both schemes use all 1681 single-shot spectra, the averaged values at each concentration x are identical. The primary distinction between SDS and ALADS lies not in the mean signal but in the measurement precision, with ALADS dramatically reducing the variance among the three measurements (Section 3.3). Both the raw Hg I intensity, $y = I_{\mathrm{HgI}}$, and the intensity ratio $y = I_{\mathrm{HgI}}/I_{\mathrm{CI}}$ increase monotonically with Hg^{2+} concentration accumulated on the SCX membrane, but the dependence is markedly nonlinear, particularly at higher concentrations. This nonlinearity arises from self-absorption of the Hg I resonance emission. The Hg I line at 253.652 nm corresponds to a transition terminating on the ground state, leaving no lower states through which the photon could relax further; therefore, photons emitted inside the plasma have a high probability of being re-absorbed by ground-state atoms. This resonance trapping produces the observed saturation. The C I line at 247.856 nm, used for normalization, originates from a non-resonant transition and is not subject to self-absorption, which explains why normalization improves precision but does not eliminate the curvature in the calibration response. To quantitatively represent this nonlinear behavior, three saturation-type calibration models were evaluated. First, the power-law model is expressed as Eq. (1).

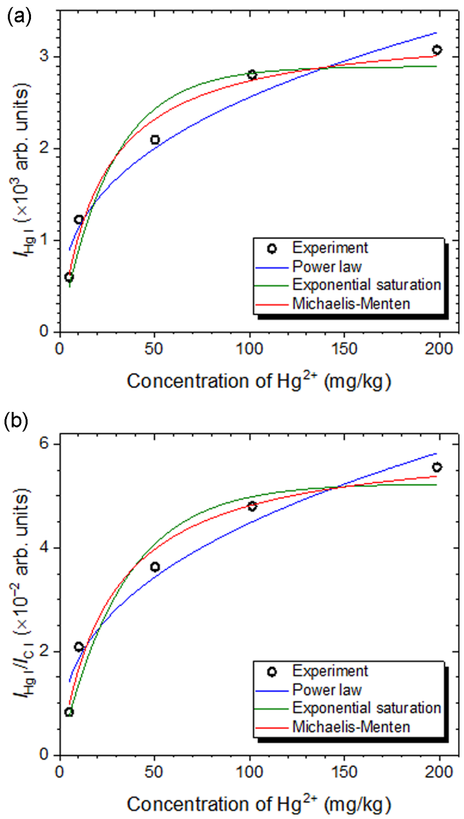

Fig. 5. Calibration curves for (a) $I_{\mathrm{Hg\,I}}$ and (b) $I_{\mathrm{Hg\,I}}/I_{\mathrm{C\,I}}$ fitted using power-law, exponential saturation, and Michaelis–Menten models.

$$y = bx^c \tag{1}$$

For the intensity data, the fitted parameters were $b = (5.0 \pm 1.3) \times 10^2$ and $c = 0.355 \pm 0.055$. For the intensity ratio, the parameters were $b = 0.0076 \pm 0.0021$ and $c = 0.384 \pm 0.059$. In both cases, the exponent $0 < c < 1$ confirms nonlinear behavior associated with self-absorption as the Hg loading increases. In these fits, any offset in y was not considered because the Hg I intensity could not be observed with the blank sample ($x = 0$). Second, the exponential saturation model is expressed as Eq. (2).

$$y = a(1 - e^{-bx}) \tag{2}$$

The parameter a represents the saturation limit, while the decay constant b governs how quickly the response approaches saturation. For the intensity data, $a = (2.89 \pm 0.23) \times 10^3$ and $b = 0.037 \pm 0.011$. For the intensity ratio, $a = 0.0524 \pm 0.0045$ and $b = 0.0300 \pm 0.0094$. Third, the Michaelis-Menten model is expressed as Eq. (3).[23,24]

$$y = \frac{y_{\max}x}{K+x} \tag{3}$$

The Michaelis–Menten formulation provides the clearest physical interpretation; $y_{\max}$ corresponds to the asymptotic intensity or intensity ratio at infinite analyte loading, and K represents the concentration at which the signal reaches half-saturation, directly linked to the onset of self-absorption. For the intensity data, $y_{\max} = 3340 \pm 20$ and $K = 22.2 \pm 5.1$. For the intensity ratio, $y_{\max} = 0.0611 \pm 0.0045$ and $K = 26.9 \pm 7.1$. Among the three models, the Michaelis–Menten fits consistently gave the highest R^2 values for both intensity and intensity ratio (*Table* 2), indicating superior representation of the saturation curvature.

LOD was also computed using the standard expression as Eq. (4).[16]

$$\mathrm{LOD} = \frac{3\sigma}{s} \tag{4}$$

In the above equation, σ represents the uncertainty in signals. Herein the standard deviation of the three measurements at the lowest concentration (5.012 mg/kg) was used in place of σ, and the sensitivity, s, was evaluated using the derivative of each fitted model at the lowest concentration (5.012 mg/kg). As above mentioned, the three measurements were obtained by both SDS and ALADS schemes. For the intensity calibration, the slopes at the lowest concentration were 59.0, 86.6, and 96.9 for the power-law, exponential, and Michaelis–Menten models, respectively, yielding LODs of 2.8, 1.9, and 1.7 mg/kg using the standard deviation from three SDS measurements and 0.47, 0.32, and 0.29 mg/kg using that from three ALADS measurements. For the intensity-ratio calibration, the slopes were 0.00103, 0.00133, and 0.00157, producing LODs of 3.0, 2.3, and 1.9 mg/kg using the standard deviation from three SDS measurements and 0.33, 0.25, and 0.21 mg/kg using that from three ALADS measurements. The complete results are summarized in *Table* 2, showing that the Michaelis–Menten model consistently provides the best calibration performance and the LOD could be remarkably decreased down by using the ALADS scheme providing highly precise measurements.

The nonlinear response observed in both the Hg I intensity and the Hg I/C I intensity ratio becomes particularly evident at higher concentrations, where the calibration curves exhibit a pronounced flattening that reflects saturation behavior. This deviation from linearity originates from self-absorption: as the laser-induced plasma becomes optically thick, photons emitted from the inner hot region of the plasma are re-absorbed by ground-state Hg atoms located in the cooler periphery. Because the Hg I 253.652 nm line terminates on the ground state and possesses a relatively large absorption coefficient, self-absorption affects this transition strongly, causing the observed

Table 2. Fitting models, y-variables, coefficients of determination (R^2), and limits of detection using SDS and ALADS ($\mathrm{LOD_{SDS}}$ and $\mathrm{LOD_{ALADS}}$, respectively)

Model	y-variable	R^2	$\mathrm{LOD_{SDS}}$ (mg/kg)	$\mathrm{LOD_{ALADS}}$ (mg/kg)
Power law	$I_{\mathrm{Hg\ I}}$	0.957	2.8	0.47
Exponential saturation	$I_{\mathrm{Hg\ I}}$	0.939	1.9	0.32
Michaelis-Menten	$I_{\mathrm{Hg\ I}}$	0.980	1.7	0.29
Power law	$I_{\mathrm{Hg\ I}}/I_{\mathrm{C\ I}}$	0.960	3.0	0.33
Exponential saturation	$I_{\mathrm{Hg\ I}}/I_{\mathrm{C\ I}}$	0.943	2.3	0.25
Michaelis-Menten	$I_{\mathrm{Hg\ I}}/I_{\mathrm{C\ I}}$	0.977	1.9	0.21

compression of sensitivity at elevated Hg loadings. The Michaelis–Menten model provides a particularly insightful framework for interpreting this behavior. For the intensity-ratio calibration, the fitted saturation level $y_{\max} = 0.0611 \pm 0.0045$ represents the maximum observable ratio when the plasma approaches a fully optically thick condition, indicating that additional Hg on the membrane cannot produce a higher measurable signal. The half-saturation constant $K = 26.9 \pm 7.1$ mg/kg identifies the concentration range at which self-absorption begins to dominate and the slope of the calibration curve decreases markedly, limiting the effective linear calibration range to roughly 20–30 mg/kg. These parameters therefore serve as direct physical indicators of the self-absorption strength and the onset of sensitivity loss.

3.5. Recovery efficiency and matrix effect

To further assess the accuracy of the LIBS–SCX quantification method, an external validation test was carried out using an independently prepared Hg^{2+} standard solution of 80.46 mg/kg. After passing this solution through the SCX membrane and performing LIBS measurements using the ALADS scheme, three intensity-ratio values were obtained: 0.04547, 0.04475, and 0.04615. These ratios were converted to concentrations using the Michaelis–Menten calibration model with $y_{\max} = 0.0611$ and $K = 26.94$ mg/kg. The resulting concentration was 78.3 ± 4.7 mg/kg. Comparing the recovered value with the known concentration (80.46 mg/kg) yields a recovery of 97.3 %.

To evaluate potential matrix effects associated with real-water samples, an additional experiment was performed using NIST SRM 1643f (Trace Elements in Water) as the sample matrix instead of ultrapure water. Unlike the calibration standards—which contained Hg^{2+} dissolved solely in ultrapure water—the SRM-based sample includes a complex mixture of inorganic ions commonly present in natural and drinking waters. These constituents may influence plasma formation, laser–sample interaction, or ion-exchange behavior of the SCX membrane, making matrix-effect verification essential for validating the applicability of the method to environmental analysis. A portion of NIST SRM 1643f was spiked with Hg^{2+} to yield a final concentration of 9.88 mg/kg. The solution was passed through a conditioned SCX membrane, dried, and analyzed by LIBS under the same conditions as the calibration standards. Using the Michaelis–Menten calibration model based on $I_{\mathrm{Hg\ I}}/I_{\mathrm{C\ I}}$, the recovered Hg^{2+} concentrations was 10.49 ± 0.34 mg/kg. This result demonstrates that the presence of common dissolved species in SRM 1643f does not significantly interfere with LIBS quantification when SCX membrane preconcentration and ALADS-based precision enhancement are employed. The recovery of approximately 106 % indicates only minor matrix influence on the measurement accuracy, while the low RSD confirms that measurement precision remains comparable to that obtained for standards prepared in ultrapure water. Thus, the proposed method exhibits strong robustness against typical water-matrix constituents and is suitable for quantitative determination of Hg^{2+} in environmental water samples. To further assess potential matrix effects, tap water was examined as an additional real-world matrix. When the unspiked tap water was passed through the SCX membrane and analyzed by LIBS, no detectable Hg emission was observed, indicating that the intrinsic Hg content of the purified water was below the method's LOD (~0.2 mg/kg). To evaluate whether the tap water matrix influences Hg recovery, the same water was spiked with 50.25 mg/kg Hg^{2+}, processed through the SCX membrane, and analyzed using the Michaelis–Menten calibration model based on $I_{\mathrm{Hg\ I}}/I_{\mathrm{C\ I}}$. The resulting concentration was 50.2 ± 1.4 mg/kg yielding a recovery of 99.9 %. These results confirm that the purified-water matrix does not introduce significant bias into the SCX–LIBS measurement process, and that the ALADS-enhanced LIBS method maintains both accuracy and precision even in non-ideal aqueous matrices. This further supports the robustness of the proposed approach for practical water-analysis applications.

4. Conclusions

This study demonstrates a high-precision and quantitative LIBS for determining inorganic Hg^{2+} in water by integrating solid-phase preconcentration on SCX membranes with ALADS. The SCX membranes exhibited intrinsic spatial inhomogeneity of Hg loading on the millimeter scale, which fundamentally limited the precision of conventional single-shot or SDS. Although normalization to the non-resonant C I line at 247.856 nm partially compensated for plasma-temperature fluctuations, it did not correct this spatial irregularity. ALADS effectively distributed the sample inhomogeneity equally across measurement groups, reducing variance among replicated measurements by approximately an order of magnitude compared with SDS. Nonlinear calibration behavior arising from strong self-absorption of the resonance Hg I line at 253.652 nm was successfully modeled using three saturation-type functions: the power-law, exponential saturation, and Michaelis–Menten models. The Michaelis–Menten formulation, in particular, provided the most physically meaningful description of the saturation effect, yielding the highest goodness of fit and the lowest limits of detection. By combining ALADS-enhanced precision with nonlinear calibration modeling, the method achieved an LOD of ~0.21 mg/kg when using the intensity ratio ($I_{\mathrm{Hg\ I}}/I_{\mathrm{C\ I}}$) and the Michaelis–Menten function. The applicability of the developed SCX–LIBS approach was further validated through recovery tests using standard solutions, NIST water CRM spiked with Hg^{2+}, and purified water samples fortified with Hg^{2+}. The results showed good agreement with the expected concentrations and demonstrated minimal matrix effects, confirming the robustness of the method for complex aqueous matrices. Overall, this work establishes ALADS-assisted LIBS combined with SCX membrane preconcentration as an effective strategy for quantitative Hg^{2+} determination in water. The approach provides substantially improved precision, reliable nonlinear calibration, and robust performance across different aqueous matrices. Although the present configuration yields a detection limit of approximately 0.2 mg/kg, the capability of the SCX membrane to quantitatively retain Hg^{2+} from substantially larger sample volumes suggests that additional preconcentration could, in principle, extend the detection capability toward the low-ppb range. Such detection levels, while not required for ultratrace environmental surveillance, are highly relevant for applications such as monitoring Hg contamination in industrial wastewater, screening effluents from mining or metallurgical processes, verifying treatment efficiency in remediation systems, and performing rapid on-site assessments where fast and portable measurements are prioritized over sub-ppb sensitivity. These considerations highlight the potential of the developed SCX–ALADS–LIBS platform as a practical and field-deployable analytical tool for routine mercury monitoring in diverse real-world scenarios.

Acknowledgements

This research was supported by Glocal University Project of Mokpo National University in 2025. Prof. Yonghoon Lee gratefully acknowledges Mr. Hanbum Choi for his technical assistance.

References

1. M. Bibi, Samiullah, F. Behlil, S. Afzal, and Sahifa, *Pure Appli. Biol.*, **12**(2), 835-847 (2023). https://dx.doi.org/10.19045/bspab.2023.120083
2. T. W. Clarkson and L. Magos, *Crit. Rev. Toxicol.*, **36**(8), 609-662 (2006). https://doi.org/10.1080/10408440600845619
3. B. F. Azevedo, L. B. Furieri, F. M. Peçanha, G. A. Wiggers, P. F. Vassallo, M. R. Simões, J. Fiorim, P. R. de Batista, M. Fioresi, L. Rossoni, I. Stefanon, M. J. Alonso, M. Salaices, and D. V. Vassallo, *J. Biomed. Biotechnol.*, **2012**, 949048 (2012). https://doi.org/10.1155/2012/949048
4. S. M. Ullrich, T. W. Tanton, and S. A. Abdrashitova, *Crit. Rev. Environ. Sci. Technol.*, **31**(3), 241-293 (2001). https://doi.org/10.1080/20016491089226
5. R. Sánchez, J. Snell, A. Held, and H. Emons, *Anal. Bioanal. Chem.*, **407**, 6569-6574 (2015). https://doi.org/10.1007/s00216-015-8833-9
6. A. A. Elezz, H. M. Hassan, H. A. Alsaadi, A. Easa, S. Al-Meer, K. Elsaid, Z. K. Ghouri, and A. Abdala, *Methods*

Protoc., **1**(3), 31 (2018). https://doi.org/10.3390/mps1030031

7. D. Sánchez-Rodas, W. T. Corns, B. Chen, and P. B. Stockwell, *J. Anal. Atom. Spectrom.*, **25**(7), 933-946 (2010). https://doi.org/10.1039/B917755H
8. S.-J. Yang, Y. Lee, and S.-H. Nam, *J. Anal. Sci. Technol.*, **13**, 45 (2022). https://doi.org/10.1186/s40543-022-00354-1
9. S.-H. Nam, N.-Y. Kim, E.-S. Park, and Y. Lee, *Bull. Korean Chem. Soc.*, **43**(3), 402-406 (2022). https://doi.org/10.1002/bkcs.12474
10. I. Dakova, T. Yordanova, and I. Karadjova, *Molecules*, **29**(1), 187 (2024). https://doi.org/10.3390/molecules29010187
11. S. Kulomäki, E. Lahtinen, S. Perämäki, and A. Väisänen, *Talanta*, **240**, 123163 (2022). https://doi.org/10.1016/j.talanta.2021.123163
12. T. Hashempur, M. K. Rofouei, and A. R. Khorrami, *Microchem. J.*, **89**(2), 131-136 (2008). https://doi.org/10.1016/j.microc.2008.01.004
13. S. H. Lee, S.-J. Yang, Y. Lee, and S.-H. Nam, *J. Anal. Sci. Technol.*, **12**, 28 (2021). https://doi.org/10.1186/s40543-021-00280-8
14. S. H. Lee, S.-W. Kwon, Y. Lee and S.-H. Nam, *J. Anal. Sci. Technol.*, **11**, 27 (2020). https://doi.org/10.1186/s40543-020-00227-5
15. F. J. Fortes, J. Moros, P. Lucena, L. M. Cabalín, and J. J. Laserna, *Anal. Chem.*, **85**(2), 640-669 (2013). https://doi.org/10.1021/ac303220r
16. D. W. Hahn and N. Omenetto, *Appl. Spectrosc.*, **66**(4), 347-419 (2012). https://doi.org/10.1366/11-06574
17. Y. Lee, *Anal. Sci. Technol.*, **37**(1), 12-24 (2024). https://doi.org/10.5806/AST.2027.37.1.12
18. J. Park, S.-H. Han, S.-H. Nam, and Y. Lee, *Appl. Spectrosc.*, **77**(12), 1351-1361 (2023). https://doi.org/10.1177/00037028231206195
19. H. Kim, Y. Jeon, W. B. Lee, S.-H. Nam, S.-H. Han, K.-S. Ham, V. K. Singh, and Y. Lee, *Appl. Spectrosc.*, **73**(10), 1172-1182 (2019). https://doi.org/10.1177/0003702819861552
20. Z. A. Umar, S. Kumar, S.-H. Han, S.-B. Ki, S. Kim, S. Jung, S.-H. Nam, and Y. Lee, *Minerals*, **15**, 659 (2025). https://doi.org/10.3390/min15060659
21. Y. Gong, D. Choi, B.-Y. Han, J. Yoo, S.-H. Han, and Y. Lee, *J. Nucl. Mater.*, **453**(1-3), 8-15 (2014). https://doi.org/10.1016/j.jnucmat.2014.06.022
22. Atomic Spectra Database, NIST Standard Reference Database 78, Version 5.12. https://www.nist.gov/pml/atomic-spectra-database
23. S. Ebel, D. Alert, and U. Schaefer, *Chromatographia*, **18**(1), 23-27 (1984). https://doi.org/10.1007/BF02279459
24. R. A. Croce Jr, S. Vaddiraju, F. Papadimitrakopoulos, and F. C. Jain, *Sensors*, **12**, 13402-13416 (2012). https://doi.org/10.3390/s121013402